# Stochastic Collocation With Non-Gaussian Correlated Process Variations: Theory, Algorithms, and Applications

Chunfeng Cui<sup>®</sup> and Zheng Zhang<sup>®</sup>, Member, IEEE

Abstract—Stochastic spectral methods have achieved a great success in the uncertainty quantification of many engineering problems, including variation-aware electronic and photonic design automation. State-of-the-art techniques employ generalized polynomial-chaos expansions and assume that all random parameters are independent or Gaussian correlated. This assumption is rarely true in real applications. How to handle non-Gaussian correlated random parameters is a long-standing and fundamental challenge: It is not clear how to choose basis functions and to perform a projection step in a correlated uncertain parameter space. This paper first presents a new set of basis functions to well capture the impact of non-Gaussian correlated parameters and then proposes an automatic and optimization-based quadrature method to perform projectionbased stochastic collocation with a few simulation samples in the correlated parameter space. We further provide some theoretical proofs for the complexity and error bound of our proposed method. The numerical experiments on several synthetic, electronic, and photonic integrated circuit examples show the nearly exponential convergence rate of our approach and its significant (700x-6000x) speedup than Monte Carlo. Many other open problems with non-Gaussian correlated uncertainties can be further solved based on this paper.

Index Terms—Design automation algorithm, integrated circuits (ICs), integrated photonics, non-Gaussian correlation, process variation, uncertainty quantification.

#### I. INTRODUCTION

PROCESS variation (e.g., random-doping fluctuations and line edge roughness) is a major concern in nanoscale fabrications [2]: Even a random difference on the atomic scale can have a large impact on the electrical properties of electronic integrated circuits (ICs) [3], causing significant performance degradation and yield reduction. This issue is more severe in photonic IC [4]–[6], as photonic IC is much more sensitive to geometric variations such as surface roughness due to its large device dimension compared with the

Manuscript received August 22, 2018; revised December 4, 2018; accepted December 16, 2018. Date of publication December 21, 2018; date of current version July 18, 2019. This work was supported in part by the NSF-CCF under Award 1763699, in part by the UCSB Start-Up Grant, and in part by Samsung Gift Funding. Recommended for publication by Associate Editor S. Grivet-Talocia upon evaluation of reviewers' comments.

The authors are with the Department of Electrical and Computer Engineering, University of California at Santa Barbara, Santa Barbara, CA 93106 USA (e-mail: chunfengcui@ucsb.edu; zhengzhang@ece.ucsb.edu).

Color versions of one or more of the figures in this paper are available online at http://ieeexplore.ieee.org.

Digital Object Identifier 10.1109/TCPMT.2018.2889266

small operation wavelength [7]. In order to address this long-standing and increasingly important issue, efficient uncertainty quantification tools should be developed to predict and control the uncertainties of chip performance under various process variations. Due to its ease of implementation, Monte Carlo (MC) [7], [8] has been used in many commercial design automation tools. However, an MC method often requires a huge number of device- or circuit-level simulation samples to achieve acceptable accuracy, and thus, it is very time-consuming. As an alternative, stochastic spectral methods [9] may achieve orders-of-magnitude speedup over MC methods in many application domains.

A stochastic spectral method approximates an unknown uncertain quantity (e.g., the nodal voltage, branch current, or power dissipation of a circuit) as a linear combination of some specialized basis functions, such as the generalized polynomial chaos [10]. Both intrusive (i.e., nonsampling) solvers (e.g., stochastic Galerkin [11] and stochastic testing [12]) and nonintrusive (i.e., sampling) solvers (e.g., stochastic collocation [13]) have been developed to compute the unknown weights of these predefined basis functions. These techniques have been successfully applied in electronic IC [14]–[23], microelectromechanical systems [24], [25], and photonic IC [26], [27] applications, achieving orders-of-magnitude speedup than MC when the number of random parameters is small or medium. In the past few years, there has been a rapid progress in developing highdimensional uncertainty quantification solvers. Representative results include tensor recovery [28], compressive sensing [29], analysis of variance or high-dimensional model representation [24], [30], [31], matrix low-rank approximation [32], stochastic model order reduction [33], and hierarchical uncertainty quantification [24], [25].

The above-mentioned existing techniques use generalized polynomial chaos [10] as their basis functions, and they assume that all process variations can be described by independent random parameters. Unfortunately, this assumption is not true in many practical cases. For instance, the geometric or electrical parameters influenced by the same fabrication step are often highly correlated. In a system-level analysis, the performance parameters from circuit-level simulations are used as the inputs of a system-level simulator, and these circuit-level performance quantities usually depend on each other due to the network coupling and feedback. In the

2156-3950 © 2018 IEEE. Personal use is permitted, but republication/redistribution requires IEEE permission. See http://www.ieee.org/publications\_standards/publications/rights/index.html for more information.

photonic IC, spatial correlations may have to be considered for almost all components due to the small wavelength [34]. All these correlations are not guaranteed to be Gaussian, and they cannot be handled by preprocessing techniques such as principal component analysis [35]. Karhunen–Loeve theorem [36], [37] and Rosenblatt transformation [38] may transform correlated parameters into uncorrelated ones, but they are error-prone and not scalable.

This paper develops new theory and algorithms of uncertainty quantification with non-Gaussian correlated process variations. Two main challenges arise when we quantify the impact of correlated non-Gaussian process variations. First, we need to develop a new set of stochastic basis functions to capture the effects of non-Gaussian correlated process variations. Soize and Ghanem [39] suggested to modify the generalized polynomial chaos, but the resulting nonpolynomial basis functions are nonsmooth and numerically unstable. Second, we need to develop a spectral method (either stochastic collocation or stochastic Galerkin) to compute the weights of the new basis functions. This requires performing a projection step by an accurate numerical integration in a multidimensional correlated parameter space. While the numerical integration in a 1-D space [40] or a 2-D correlated square space [41] is wellstudied, accurate numerical integration in a higher dimensional correlated parameter space remains a challenge. During the preparation of this paper, we noticed some recent results on stochastic Galerkin [42], [43] and sensitivity analysis for dependent random parameters [44]. However, the theoretical analysis and numerical implementation of stochastic collocation have not been investigated for systems with non-Gaussian correlated parameters.

*Main Contributions:* This paper presents a novel stochastic collocation approach for systems with correlated non-Gaussian uncertain parameters. Our main contributions include the following.

- 1) The development of a set of basis functions that can capture the impact of non-Gaussian correlated process variations. Some numerical implementation techniques are also presented to speed up the computation.
- 2) An optimization-based quadrature rule to perform projection in a multidimensional correlated parameter space. The previous stochastic spectral methods use id [45] or Gauss quadrature [40], which is not applicable for non-Gaussian correlated cases. We reformulate the numerical quadrature problem as a nonlinear optimization problem and apply a block coordinate descent method to solve it. Our approach can automatically determinate the number of quadrature samples. We also provide a theoretical analysis for the upper and lower bounds of the number of quadrature samples required in our framework.
- 3) Theoretical error bound of our algorithm. We show that the following holds.
  - a) We can obtain the exact solution under some mild conditions when the stochastic solution is a polynomial function.

# TABLE I NOTATIONS IN THIS PAPER

number of random parameters describing process variations

the highest total polynomial order

P	and ingress town porjustinal state.
M	number of quadrature nodes
ξ	a vector denoting d uncertain parameters
$\rho(\boldsymbol{\xi})$	the joint probability density function of $\boldsymbol{\xi}$
$\boldsymbol{\xi}_k$	the value of $\xi$ at a quadrature node
$w_k$	nonnegative weight associated with $\boldsymbol{\xi}_k$
$\mathbf{w}$	$d$ -dimensional vector of $w_k$
$\mathbf{e}_1$	a vector of the form $[1,0,\ldots,0]^T$
$\alpha$	d-dimensional vector indicating order of a multivariate polynomial
$\Psi_{\alpha}(\boldsymbol{\xi})$	orthonormal basis functions with $\mathbb{E}[\Psi_{\alpha}(\xi)\Psi_{\beta}(\xi)] = \delta_{\alpha\beta}$
$c_{\alpha}$	coefficient or weight of $\Psi_{\alpha}(\xi)$ in the expansion
$\tilde{c}_{oldsymbol{lpha}}$	approximation for $c_{\alpha}$ by numerical integration
$c_{m{lpha}} \ \tilde{c}_{m{lpha}} \ \Psi_j(m{\xi})$	$\Psi_{\alpha}(\boldsymbol{\xi})$ in the graded lexicographic order
$c_{j}$	coefficient or weight of $\Psi_j(\boldsymbol{\xi})$ in the expansion
$ ilde{c}_j$	approximation for $c_j$ by numerical integration
$egin{array}{c} c_j \  ilde{c}_j \ y(oldsymbol{\xi}) \end{array}$	the unknown stochastic solution to be computed
$\tilde{y}(\boldsymbol{\xi})$	approximation of $y(\boldsymbol{\xi})$ by our method
$y_p(oldsymbol{\xi}) \ \mathcal{S}_p$	the projection of $y(\boldsymbol{\xi})$ onto polynomial set $\mathcal{S}_p$
	the set of d-dimensional polynomials with total order $\leq p$
$N_p$	the number of d-dimensional monomials with order $\leq p$

- b) For a general smooth stochastic solution, an upper error bound exists for our stochastic collocation algorithm, and it depends on the distance of the unknown solution to a polynomial set as well as the numerical error of our optimization-based quadrature rule.
- 4) A set of numerical experiments on synthetic and realistic electronic and photonic IC examples. The results show the fast convergence rate of our method and its orders-of-magnitude (700×-6000×) speedup than MC.

Before discussing about the technical details, we summarize some of the frequently used notations in Table I.

#### II. PRELIMINARIES

#### A. Review of Stochastic Collocation

Stochastic collocation [13], [45]–[47] is the most popular nonintrusive stochastic spectral method. The key idea is to approximate the unknown stochastic solution as a linear combination of some specialized basis functions and to compute the weights of all basis functions based on a postprocessing step such as projection. In order to implement the projection, one needs to do some device- or circuit-level simulations repeatedly for some parameter samples selected by a quadrature rule. Given a good set of basis functions and an accurate quadrature rule, stochastic collocation may obtain a highly accurate result with only a few repeated simulations and can achieve orders-of-magnitude speedup than MC when the number of random parameters is small or medium.

Specifically, let  $\xi = [\xi_1, \dots, \xi_d]^T \in \mathbb{R}^d$  denote a set of random parameters that describe some process variations. We aim to estimate the uncertainty of  $y(\xi)$ , which is a parameter-dependent output of interest such as the power dissipation of a memory cell, the 3-dB bandwidth of an amplifier, or the frequency of an oscillator. In almost all chip design cases, we do not have a closed-form expression of  $y(\xi)$ , and we have to call a time-consuming device- or circuit-level simulator (which involves solving large-scale differential equations) to obtain the numerical value of  $y(\xi)$  for each specified sample

of  $\xi$ . Stochastic spectral methods aim to approximate  $y(\xi)$  via

$$y(\xi) \approx \sum_{|\alpha|=0}^{p} c_{\alpha} \Psi_{\alpha}(\xi), \text{ with } \mathbb{E}[\Psi_{\alpha}(\xi) \Psi_{\beta}(\xi)] = \delta_{\alpha,\beta}$$
 (1)

where  $\mathbb{E}$  denotes the expectation operator,  $\delta$  denotes a Delta function, and the basis functions  $\{\Psi_{\alpha}(\xi)\}$  are some orthonormal basis functions indexed by a vector  $\alpha = [\alpha_1, \dots, \alpha_d] \in \mathbb{N}^d$ . The total order of the basis function  $|\alpha| = \alpha_1 + \dots + \alpha_d$  is bounded by p, and thus, the total number of basis functions is

$$N_p = \binom{p+d}{d} = (p+d)!/(p!d!).$$
 (2)

The coefficient  $c_{\alpha}$  can be obtained by a projection

$$c_{\alpha} = \mathbb{E}[y(\xi)\Psi_{\alpha}(\xi)] = \int_{\mathbb{R}^d} y(\xi)\Psi_{\alpha}(\xi)\rho(\xi)d\xi \tag{3}$$

where  $\rho(\xi)$  is the joint probability density function. The integral in (3) needs to be evaluated with numerical integration

$$c_{\alpha} \approx \sum_{k=1}^{M} y(\boldsymbol{\xi}_{k}) \Psi_{\alpha}(\boldsymbol{\xi}_{k}) w_{k} \tag{4}$$

where  $\{\xi_k\}_{k=1}^M$  are the quadrature nodes and  $\{w_k\}_{k=1}^M$  are the corresponding quadrature weights. The key of stochastic collocation is to choose proper basis functions and an excellent quadrature rule, such that M is as small as possible in (4).

#### B. Existing Solutions for Independent Cases

Most existing stochastic spectral methods assume that  $\boldsymbol{\xi} = [\xi_1, \dots, \xi_d]^T$  are mutually independent. In this case, given the marginal density function  $\rho_k(\xi_k)$  of each parameter, the joint density function is  $\rho(\boldsymbol{\xi}) = \Pi_{k=1}^d \rho_k(\xi_k)$ . Consequently, an excellent choice of basis functions is the generalized polynomial chaos [10]: The multivariate basis function is obtained as the product of some univariate polynomial basis functions

$$\Psi_{\alpha}(\boldsymbol{\xi}) = \phi_{1,\alpha_1}(\xi_1) \dots \phi_{d,\alpha_d}(\xi_d). \tag{5}$$

Here, each univariate basis function  $\phi_{k,a_k}(\xi_k)$  can be constructed via the well-known three-term recurrence relation [48], and the univariate basis functions of the same parameter  $\xi_k$  are mutually orthonormal with respect to the marginal density function  $\rho_k(\xi_k)$ .

When  $\xi$  are mutually independent, the quadrature points and weights in (4) are often constructed via the tensor product of 1-D quadrature points and weights. Specifically, let  $\{\xi_{i_k}, w_{i_k}\}$  be the quadrature nodes and weights for a parameter  $\xi_k$  (for instance, via Gaussian quadrature rule [40]) and  $\xi_{i_1...i_d} = [\xi_{i_1}, \ldots, \xi_{i_d}]^T$  and  $w_{i_1...i_d} = w_{i_1} \ldots w_{i_d}$  be the quadrature points and weights for a d-dimensional problem. Another popular approach is the sparse grid technique [45], [49]–[51], which can significantly reduce the number of quadrature points by exploiting the nested structure of the quadrature points of different accuracy levels.

#### C. Non-Gaussian Correlated Cases

In general,  $\xi$  can be non-Gaussian correlated, and the joint density  $\rho(\xi)$  cannot be written as the product of the individual marginal density functions. As a result, the multivariate basis function cannot be obtained as in (5). It is also hard to choose a small number of quadrature nodes  $\{\xi_k\}$  and weights  $\{w_k\}$  that can produce highly accurate integration results.

In order to quantify the impact of non-Gaussian correlated uncertainties, Soize and Ghanem [39] suggested a set of non-smooth orthonormal basis functions by modifying the generalized polynomial chaos [10]. The modified basis functions were employed in [26] for the variability analysis of silicon photonic devices. However, the algorithm does not converge well due to the numerical instability of the basis functions, and designers cannot easily extract statistical information (e.g., mean value and variance) from the obtained solution. In the applied math community, multivariate orthogonal polynomials may be constructed via the multivariate three-term recurrence [52], [53]. However, the theories in [54] and [55] either are hard to implement or can only guarantee weak orthogonality.

#### III. PROPOSED ORTHONORMAL BASIS FUNCTIONS

This section presents a set of smooth orthonormal basis functions that can capture the impact of non-Gaussian correlated random parameters. The proposed basis functions allow us to approximate a smooth  $y(\xi)$  with a high accuracy and to extract its statistical moments analytically or semianalytically.

#### A. Generating Multivariate Orthonormal Polynomials

We adopt a Gram–Schmidt approach to calculate the basis functions recursively. The Gram–Schmidt method was used for vector orthogonalization in the Euclidean space [54]. It can also be generalized to construct some orthogonal polynomial functions. The key difference here is to replace the vector inner product with the functional expectations.

Specifically, we first reorder the monomials  $\xi^{\alpha} = \xi_1^{\alpha_1} \dots \xi_d^{\alpha_d}$  in the graded lexicographic order and denote them as  $\{p_j(\xi)\}_{j=1}^{N_p}$ . For instance, when d=2 and p=2, there is

$$\{p_j(\xi_1, \xi_2)\}_{j=1}^6 = \{1, \xi_1, \xi_2, \xi_1^2, \xi_1 \xi_2, \xi_2^2\}.$$

Then, we set  $\Psi_1(\xi) = 1$  and generate orthonormal polynomials  $\{\Psi_j(\xi)\}_{j=1}^{N_p}$  in the correlated parameter space recursively by

$$\hat{\Psi}_{j}(\xi) = p_{j}(\xi) - \sum_{i=1}^{j-1} \mathbb{E}[p_{j}(\xi)\Psi_{i}(\xi)]\Psi_{i}(\xi)$$
 (6)

$$\Psi_j(\boldsymbol{\xi}) = \frac{\hat{\Psi}_j(\boldsymbol{\xi})}{\sqrt{\mathbb{E}[\hat{\Psi}_j^2(\boldsymbol{\xi})]}}, \quad j = 2, \dots, N_p.$$
 (7)

The basis functions defined by this approach are unique under the specific order of monomials. If the ordering of monomials is changed, one can get another set of basis functions. Since the basis functions are orthonormal polynomials, we can easily extract the mean value and statistical moment of an approximated stochastic solution.

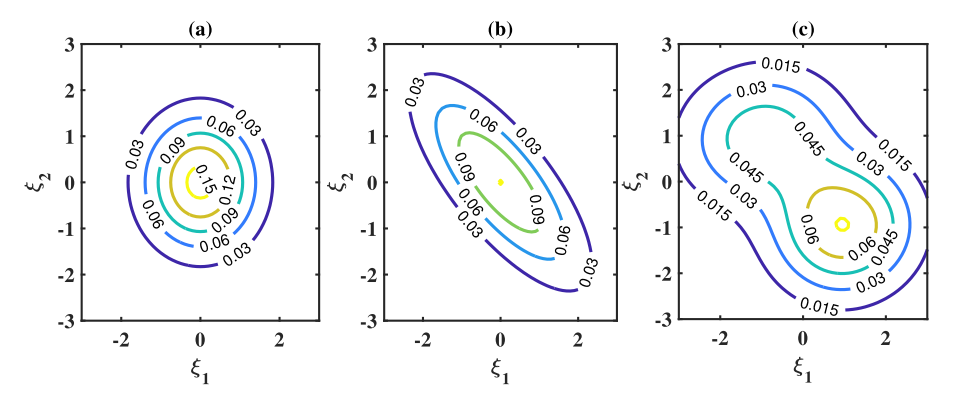


Fig. 1. Several joint density functions. (a) Independent Gaussian. (b) Correlated Gaussian. (c) Correlated non-Gaussian (e.g., a Gaussian mixture distribution).

Recently, we have also proposed the basis function construction method via a Cholesky decomposition [55], which is easy to implement and suitable for high-dimensional cases. However, the resulting basis functions can be occasionally inaccurate due to the numerical instability of the Cholesky factorization on large ill-conditioned covariance matrices. This paper focuses on the fundamental theory of stochastic collocation for correlated cases, and therefore, we employ the Gram–Schmidt method.

#### B. Numerical Implementation Issues

The main challenge in the basis function generation is to compute the expectations in a correlated parameter space, which involves evaluating the moments  $\mathbb{E}[\xi^{\alpha}]$  up to order 2p. Some techniques can be used to speed up the computation.

In practice, the process variations are generally described by a set of measurement data from testing chips, and their joint density function  $\rho(\xi)$  is fit using some density estimators. A widely used model is the Gaussian mixture

$$\rho(\xi) = \sum_{i=1}^{n} r_i \mathcal{N}(\xi | \mu_i, \Sigma_i), \text{ with } r_i > 0, \sum_{i=1}^{n} r_i = 1$$
 (8)

where  $\mathcal{N}(\boldsymbol{\xi}|\boldsymbol{\mu}_i, \Sigma_i)$  denotes a multivariate Gaussian distribution with mean  $\boldsymbol{\mu}_i \in \mathbb{R}^d$  and a covariance matrix  $\Sigma_i \in \mathbb{R}^{d \times d}$ . Fig. 1 compares the Gaussian mixture model with independent and correlated Gaussian distributions. With a Gaussian mixture, the moments can be computed accurately using a functional tensor-train approach (see [57, Sec. III-C]).

For general cases, one may estimate the moments by changing the variables and density function

$$\mathbb{E}[\boldsymbol{\xi}^{\boldsymbol{\alpha}}] = \int_{\mathbb{R}^d} g_{\boldsymbol{\alpha}}(\boldsymbol{\eta}) \hat{\rho}(\boldsymbol{\eta}) d\boldsymbol{\eta}, \text{ with } g_{\boldsymbol{\alpha}}(\boldsymbol{\eta}) = \frac{\boldsymbol{\eta}^{\boldsymbol{\alpha}} \rho(\boldsymbol{\eta})}{\hat{\rho}(\boldsymbol{\eta})}$$
(9)

where  $\hat{\rho}(\eta)$  denotes the joint density function of independent random parameters  $\eta \in \mathbb{R}^d$ . Then, standard quadrature methods, such as sparse grid [45] or tensor-product Gauss quadrature, can be used to evaluate the integration. The tensor-train-based method in [25] can be used to reduce the integration cost when d is large. The potential limitation is that it may be nontrivial to obtain highly accurate results if  $g_{\alpha}(\eta)$  is highly nonlinear or even nonsmooth. Note that we only need to use a high-order quadrature rule in an independent

parameter space and repeatedly evaluate some cheap closedform functions here, and we do not need to perform expensive device or circuit simulations when we compute the basis functions.

In this paper, we use Gaussian mixture models to describe non-Gaussian correlated uncertainties and employ the functional tensor-train method [55] for moment computation.

#### IV. OPTIMIZATION-BASED QUADRATURE

After constructing the basis functions, we still need to choose a small number of the quadrature nodes and weights in order to calculate  $c_{\alpha}$  by (4) with a small number of deviceor circuit-level simulations. Motivated by [58] and [59], we present an optimization model to decide a proper quadrature rule. Our method differs from [58] and [59] in both algorithm framework and theoretical analysis. First, while [56] only updates the quadrature weights by linear programing, we optimize the quadrature samples and weights by nonlinear optimization. Second, our optimization setup differs from that in [57]: We minimize the integration error of our proposed multivariate orthonormal basis functions, such that the resulting quadrature rule is suitable for quantifying the impact of non-Gaussian correlated uncertainties. Third, we handle the nonnegative constraint of the weight w and the nonlinear objective function of  $\bar{\xi}$  separately via a block coordinate descent approach. Fourth, we propose a novel initializing method via weighted complete-linkage clustering. Finally, we present the theoretical results regarding the algorithm complexity and error bound. Our method is summarized in Algorithm 1, and we elaborate the key ideas in the following.

#### A. Optimization Model of Our Quadrature Rule

Our idea is to compute a set of quadrature points and weights that can accurately estimate the numerical integration of some testing functions. Given a joint density function  $\rho(\xi)$ , we seek for the quadrature nodes and weights  $\{\xi_k, w_k\}_{k=1}^M$  by matching the integration of basis functions up to order 2p

$$\mathbb{E}[\Psi_j(\boldsymbol{\xi})] = \int_{\mathbb{R}^d} \Psi_j(\boldsymbol{\xi}) \rho(\boldsymbol{\xi}) d\boldsymbol{\xi} = \sum_{k=1}^M \Psi_j(\boldsymbol{\xi}_k) w_k,$$

$$\forall j = 1, \dots, N_{2n}$$
 (10)

#### Algorithm 1 Proposed Stochastic Collocation Method

- Step 1 Initialize the quadrature nodes and weights via Algorithm 3.
- Step 2 **Increase phase.** Update the quadrature nodes and weights by solving (11). If Alg. 2 fails to converge, increase the node number and go back to Step 1.
- Step 3 **Decrease phase.** Decrease the number of nodes, and update them by solving (11). Repeat Step 3 until no points can be deleted [in other words, the objective function of (11) fails to reduce below a prescribed threshold]. Return the nodes and weights.
- Step 4 Call a deterministic simulator to compute  $\{y(\xi_k)\}_{k=1}^M$ . Then compute the coefficients  $\{c_{\alpha}\}$  via (4).

**Output**: The coefficients  $\{c_{\alpha}\}$  in (1).

where  $N_{2p} = {2p+d \choose d}$  denotes the total number of basis functions with their total order bounded by 2p.

We choose the above-mentioned testing functions based on two reasons. First, it is easy to show that  $\mathbb{E}[\Psi_j(\xi)] = \mathbb{E}[\Psi_j(\xi)\Psi_1(\xi)] = \delta_{1j}$ . Second, we can show that for any polynomial function  $f(\xi)$  bounded by order 2p, the integration of  $f(\xi)$  weighted by the density function  $\rho(\xi)$  (i.e.,  $\mathbb{E}[f(\xi)]$ ) can be written as the weighted sum of  $\mathbb{E}[\Psi_j(\xi)]$ 's, and therefore, one can get the exact integration result if (10) holds. In stochastic collocation, if  $y(\xi)$  is a polynomial function bounded by order p, then  $c_{\alpha} = \mathbb{E}[y(\xi)\Psi_{\alpha}(\xi)]$  can be accurately computed for *every* basis function with  $|\alpha| \leq p$  if (10) holds. The detailed derivations are given in Theorem 2 (see Section V).

In practice, we propose to rewrite (10) as the following nonlinear least-square problem:

$$\min_{\bar{\boldsymbol{\xi}}, \mathbf{w} \ge 0} \|\Phi(\bar{\boldsymbol{\xi}})\mathbf{w} - \mathbf{e}_1\|_2^2 \tag{11}$$

where  $\bar{\boldsymbol{\xi}} = [\boldsymbol{\xi}_1^T, \dots, \boldsymbol{\xi}_M^T]^T \in \mathbb{R}^{Md}$ ,  $\mathbf{w} = [w_1, \dots, w_M]^T \in \mathbb{R}^M$ ,  $\mathbf{e}_1 = [1, 0, \dots, 0]^T \in \mathbb{R}^{N_{2p}}$ ,  $\Phi(\bar{\boldsymbol{\xi}})$  is a matrix of size  $N_{2p} \times M$  with the (j, k)th element being  $(\Phi(\bar{\boldsymbol{\xi}}))_{jk} = \Psi_j(\boldsymbol{\xi}_k)$ , and  $\|\cdot\|_2$  denotes the Euclidean norm. Here, we also require the quadrature weights to be nonnegative. This requirement is a natural extension of the 1-D Gauss quadrature rule [40], and it can help our theoretical analysis in Section V.

#### B. Block Coordinate Descent Solver for (11)

The total number of unknowns in (11) is M(d+1), which becomes large as d increases. In order to improve the scalability of our algorithm, we solve (11) by a block coordinate descent method. The idea is to update the parameters block-by-block: At the tth iteration, we first fix  $\bar{\xi}^{t-1}$  and solve a  $\mathbf{w}$ -subproblem to update  $\mathbf{w}^t$ , and then fix  $\mathbf{w}^t$  and solve a  $\boldsymbol{\xi}$ -subproblem to update  $\bar{\boldsymbol{\xi}}^t$ .

 $\xi$ -subproblem to update  $\bar{\xi}^t$ . 1) w-Subproblem: If  $\bar{\xi}^{t-1} = [\xi_1^{t-1}; \dots; \xi_M^{t-1}]$  is fixed, then (11) reduces to a convex linear least-square problem

$$\mathbf{w}^{t} = \arg\min_{\mathbf{w} \ge 0} \|\Phi(\bar{\boldsymbol{\xi}}^{t-1})\mathbf{w} - \mathbf{e}_{1}\|_{2}^{2}.$$
 (12)

#### **Algorithm 2** Block Coordinate Descent Solver for (11)

**Input**: Initial quadrature nodes  $\xi_1, \dots, \xi_M$ , the maximal iteration  $n_{\max}$ , and the tolerance  $\epsilon$ .

for  $t = 1, ..., n_{\text{max}}$  do

Update the weights  $\mathbf{w}^t$  via solving (12);

Update the nodes  $\bar{\boldsymbol{\xi}}^t$  via solving (13);

if  $\|\Phi(\bar{\boldsymbol{\xi}}^t)\mathbf{w}^t - \mathbf{e_1}\|_1 \le \epsilon$  is satisfied then

break:

**Output**: Optimal nodes and weights  $\{\xi_k, w_k\}_{k=1}^M$ .

2)  $\xi$ -Subproblem: When  $\mathbf{w}^t$  is fixed, we apply the Gaussian–Newton method to update the quadrature samples

$$\boldsymbol{\xi}_{k}^{t} = \boldsymbol{\xi}_{k}^{t-1} + \mathbf{d}_{k}^{t}, \text{ with } \{\mathbf{d}_{k}^{t}\} = \arg\min_{\{\mathbf{d}_{k}\}} \left\| \sum_{k=1}^{M} \mathbf{G}_{k}^{t} \mathbf{d}_{k} + \mathbf{r}^{t} \right\|_{2}^{2}$$

$$\tag{13}$$

where  $\mathbf{r}^t = \Phi(\bar{\boldsymbol{\xi}}^{t-1})\mathbf{w}^t - \mathbf{e}_1 \in \mathbb{R}^{N_{2p}}$  denotes the residual and  $\mathbf{G}_k^t \in \mathbb{R}^{N_{2p} \times d}$  is the Jacobian matrix of  $\mathbf{r}^t$  with respect to  $\boldsymbol{\xi}_k^{t-1}$ . In practice, we run the step in (13) once and go back to the **w**-step. This is actually the inexact block coordinate approach [58]. The pseudocodes of our block coordinate descent solver are summarized in Algorithm 2. Here, we use an  $\ell_1$ -norm in the stopping criteria since it enables us to bound the error of our whole framework in Section V.

We note that some other approaches can also solve the nonconvex optimization problem (11). When the number of unknown variables is small, we can obtain a globally optimal solution via the polynomial optimization solver based on a semidefinite positive relaxation [59]. The Levenberg–Marquardt approach or the trust region algorithm [60] can also be used to solve the  $\xi$ -subproblem, but they are more expensive than our solver. Our optimization solver converges very well in practice. As will be shown in Section V, our stochastic collocation framework actually does not necessarily require a locally or globally optimal solution of (11) at all. Instead, it only requires the objective function to be sufficiently small at the obtained quadrature samples and weights.

#### C. Initializing Quadrature Nodes and Weights

The nonlinear least-square problem (11) is nonconvex, and generally, it is hard to obtain the global optimal solution. In practice, accurate results can be obtained once we can use good initial guesses for the quadrature nodes and weights.

In Step 3 of Algorithm 1, we need to find a quadrature rule with fewer nodes after some pairs of quadrature samples and weights have already been calculated. In this case, we can simply delete one node with the smallest weigh and choose all other samples and their corresponding weights as the initial condition for the subsequent optimization problem.

In Step 1 of Algorithm 1, we need to generate some initial nodes from scratch. We first generate  $M_0 \gg M$  nodes via MC. In MC sampling, all samples have the same weights  $1/M_0$ . In order to improve the convergence, we keep all samples unchanged, but refine their weights by solving the

w-subproblem in (12). These  $M_0$  initial nodes are then grouped into M clusters, and the resulting cluster centers are set as the initial samples for whole nonlinear least-square optimization problem. This choice of initial guess proves to work very well in practice because MC itself is an integration rule with statistical accuracy guarantees.

Clustering is a classical technique in pattern recognition and data mining [61], and it gathers data with a similar pattern into one group. A widely used algorithm is hierarchical clustering. At the beginning, each single data point is a cluster by its own, and then two clusters with "the minimal distance" are merged into one single cluster sequentially. Consequently, the number of clusters is decreased by one in each iteration until the prescribed number of clusters is reached. The widely used hierarchical approaches include single linkage, complete linkage, and average linkage. They mainly differ in the criterion of choosing "the distance." The complete-linkage clustering chooses the distance between two clusters  $C_i$  and  $C_j$  as

$$D_{ij}^{0} = \max_{\xi_{1} \in C_{i}, \xi_{2} \in C_{j}} d(\xi_{1}, \xi_{2})$$

where  $d(\xi_1, \xi_2) = ||\xi_1 - \xi_2||_2$ . In our problem, the sample points are equipped with some weight parameters, and therefore, we modify the complete-linkage clustering and consider a weighted clustering problem.

1) Weighted Complete-Linkage Clustering: We define the weighted distance as

$$D_{ij} = (w_i + w_j) \left( \max_{\boldsymbol{\xi}_1 \in C_i, \boldsymbol{\xi}_2 \in C_i} d(\boldsymbol{\xi}_1, \boldsymbol{\xi}_j) \right)$$
(14)

where  $w_i = \sum_{\xi_k \in C_i} w(\xi_k)$  is the weight of the *i*th cluster. The above-mentioned distance considers both the geometric distance and the weights of different clusters. The intuition behind (14) is that we do not want a sample with a very small weight to form a cluster by itself. This algorithm tends to group a sample with a very small weight with its nearest

Once the number of clusters reduces to M, we stop the iterations and return the weight and cluster center as

$$w_{i} = \sum_{\xi_{k} \in C_{i}} w(\xi_{k}), \quad \xi_{i} = \sum_{\xi_{k} \in C_{i}} \frac{w(\xi_{k})}{w_{i}} \xi_{k} \quad \forall i = 1, \dots, M.$$
(15)

Algorithm 3 has summarized the pseudocodes of our clustering method used to initialize Algorithm 1.

#### D. Number of Quadrature Points

A fundamental question is: How many quadrature samples are necessary in order to achieve a desired level of accuracy? This question is well answered in the 1-D Gauss quadrature rule: p quadrature points provide an exact result for the numerical integration of any polynomial function bounded by order 2p - 1 [40]. However, there is no similar result for general multidimensional correlated cases.

Let  $S_{2p}$  denote all polynomial functions of  $\xi$  with their total orders bounded by 2p. The integration rule  $\{\xi_k, w_k\}_{k=1}^M$ 

Algorithm 3 Weighted Complete-Linkage Clustering

**Input**: The number of cluster M, and  $M_0 = 3M$  initial nodes  $\xi_1, \dots, \xi_{M_0}$ . Calculate the weights for  $\xi_1, \dots, \xi_{M_0}$  by solving (12).

for  $m = M_0, ..., M + 1$  do

Update the distance matrix by (14).

Find two clusters with the minimal distance, and merge them into one single cluster.

Calculate the cluster centers and weights via (15).

**Output**: Clustered nodes and weights  $\{\xi_k, w_k\}_{k=1}^M$ .

has a 2pth-order accuracy if (10) is satisfied. Here, the 2pthorder accuracy means that  $\sum_{k=1}^{M} f(\xi_k)w_k = \mathbb{E}[f(\xi)]$  for any  $f(\xi) \in \mathcal{S}_{2p}$ . We have the following result on the number of quadrature samples in order to ensure the 2 pth-order accuracy.

Theorem 1: Assuming that M pairs of quadrature samples and weights are obtained from (10) to ensure the 2pth-order integration accuracy, then the number of quadrature points satisfies  $N_p \leq M \leq N_{2p}$ .

While there exists at least one M in  $[N_p, N_{2p}]$  such that the 2pth-order integration accuracy can be achieved, we can have multiple choices of M and may even have multiple choices of quadrature samples and weights for each M. In our stochastic collocation framework, we only require one (among possibly multiple) set of quadrature samples and weights with a sufficiently small M.

In practice, we try to get a better solution by generating a better initial guess. We do this by first generating  $6N_p$ random samples via MC and grouping them into  $2N_p$  clusters. These  $M = 2N_p$  samples are used as the initial quadrature points. Then, we increase or decrease M via Algorithm 1. This process is illustrated via a 2-D example in Fig. 2. The practical number of quadrature nodes used by our stochastic collocation framework is very close to the theoretical lower bound, which is experimentally shown in Section VI-E.

#### V. Theoretical Error Bounds

In this section, we provide several theoretical results regarding the numerical accuracy of our proposed stochastic collocation algorithm for non-Gaussian correlated cases.

#### A. Conditions for Exact Results

Theorem 2 shows that our quadrature rule (10) can provide the exact results if  $y(\xi)$  satisfies certain conditions.

Theorem 2: Suppose that  $y(\xi) \in \mathcal{S}_p$  is a polynomial function bounded by order p, i.e., there exist some coefficients  $\{c_{\alpha}\}$ such that  $y(\xi) = \sum_{|\alpha|=0}^{p} c_{\alpha} \Psi_{\alpha}(\xi)$ . Denote the approximated expansion obtained via our numerical integration as

$$\tilde{y}(\xi) = \sum_{|\alpha|=0}^{p} \tilde{c}_{\alpha} \Psi_{\alpha}(\xi), \text{ with } \tilde{c}_{\alpha} = \sum_{k=1}^{M} y(\xi_{k}) \Psi_{\alpha}(\xi_{k}) w_{k}.$$
 (16)

Then,  $y(\xi)$  can be recovered exactly, i.e.,  $y(\xi) = \tilde{y}(\xi)$ , if  $\{\boldsymbol{\xi}_k, w_k\}$  satisfies (10) strictly for all  $j = 1, \dots, N_{2p}$ .

*Proof:* The detailed proof is provided in Appendix B.  $\square$  In practice, we may not be able to get an exact solution because of two reasons: 1)  $y(\xi)$  is not a polynomial in  $S_p$ ; and 2) the quadrature points and weights obtained by our numerical nonlinear optimization solver cause a small residual in (10). In this case, we can provide an error bound for our solution when  $y(\xi)$  is smooth enough and when the nonlinear optimization problem (11) is solved with certain accuracy (i.e., when the resulting objective function is below a threshold).

#### B. Three Weak Assumptions

In order to provide a theoretical analysis for the numerical error caused by  $y(\xi)$  and the nonlinear optimization solver, we make the following weak assumptions.

Assumption 1:  $y(\xi)$  is squared integrable. In other words, there exists a positive scalar L such that

$$\|y(\xi)\|_2 = \sqrt{\mathbb{E}[y^2(\xi)]} \le L.$$
 (17)

Let  $y_p(\boldsymbol{\xi}) = \arg\min_{\hat{y}(\boldsymbol{\xi}) \in \boldsymbol{\mathcal{S}}_p} \|y(\boldsymbol{\xi}) - \hat{y}(\boldsymbol{\xi})\|_2$  be the projection of  $y(\boldsymbol{\xi})$  onto  $\boldsymbol{\mathcal{S}}_p$ , and assume that there exists  $\delta$  such that

$$0 \le \|y(\xi) - y_p(\xi)\|_2 \le \delta. \tag{18}$$

Actually,  $y_p(\xi)$  can be written as  $y_p(\xi) = \sum_{|\alpha|=0}^p c_\alpha \Psi_\alpha(\xi)$ , where  $c_\alpha = \mathbb{E}[y(\xi)\Psi_\alpha(\xi)]$ .

Assumption 2: Define the numerical integration operator

$$\mathbb{I}[y(\boldsymbol{\xi})] = \sum_{k=1}^{M} y(\boldsymbol{\xi}_k) w_k. \tag{19}$$

We assume that the operator  $\mathbb{I}[y(\xi)]$  is bounded, i.e., there exists W > 0 such that

$$|\mathbb{I}[y(\xi)]| \le W \|y(\xi)\|_1$$
, where  $\|y(\xi)\|_1 = \mathbb{E}[|y(\xi)|]$ . (20)

Assumption 3: The nonlinear least-square problem (11) is solved with an error threshold  $\epsilon \geq 0$ , i.e.,

$$\|\Phi(\bar{\boldsymbol{\xi}})\mathbf{w} - \mathbf{e}_1\|_1 < \epsilon \tag{21}$$

where  $\|\cdot\|_1$  denotes the  $\ell_1$  norm in the Euclidean space. Here, the jth element in the vector  $\Phi(\bar{\boldsymbol{\xi}})\mathbf{w} - \mathbf{e_1}$  actually can be written as  $\mathbb{I}[\Psi_j(\boldsymbol{\xi})] - \mathbb{E}[\Psi_j(\boldsymbol{\xi})]$ .

#### C. Error Bound of the Proposed Stochastic Collocation

Theorem 3: Suppose that Assumptions 1–3 hold, and then numerical integration error satisfies

$$|\mathbb{E}[y(\xi)] - \mathbb{I}[y(\xi)]| \le L\epsilon + W\delta \tag{22}$$

where L is the upper bound of  $||y(\xi)||_2$  in (17), W is the upper bound of the numerical integration  $\mathbb{I}[y(\xi)]$  in (20),  $\epsilon$  is the numerical error of our nonlinear optimization solver defined in (21), and  $\delta$  is the distance from  $y(\xi)$  to  $\mathcal{S}_p$  in (18).

Based on Theorem 3, we can further derive an upper bound for the following approximation error.

Theorem 4: With Assumptions 1–3, the numerical error of our stochastic collocation algorithm satisfies

$$\|y(\xi) - \tilde{y}(\xi)\|_2 \le \delta + N_p(LT\epsilon + W\delta) \tag{23}$$

where  $T = \max_{j,l=1,...,N_{2p}} \|\Psi_j(\xi)\Psi_l(\xi)\|_2$ .

Proof: See Appendix D for the details.

Remarks: Theorem 4 indicates the following intuitions.

1) If the nonlinear optimization solver is accurate enough and  $\epsilon$  is very small, the error of our stochastic collocation is dominated by the approximation error  $\delta$ .

- 2) As we increase the order of basis functions,  $\delta$  decreases and the result becomes more and more accurate.
- 3) If the total order of the basis function is very high and  $\delta$  becomes extremely small, the optimization error  $\epsilon$  will dominate the overall numerical error, and the convergence will slow down.

Once (10) holds, we should have the following result:

$$\mathbb{I}[\Psi_i(\boldsymbol{\xi})\Psi_j(\boldsymbol{\xi})] = \sum_{k=1}^M \Psi_i(\boldsymbol{\xi}_k)\Psi_j(\boldsymbol{\xi}_k)w_k = \delta_{i,j}.$$

In practice, there are numerical errors caused by quadrature points and weights obtained by the optimization solver. In Lemma 1, we show that the error is bounded.

Lemma 1: Suppose that Assumptions 1–3 hold, and define a matrix  $\mathbf{V} \in \mathbb{R}^{N_p \times N_p}$  with each element  $\mathbf{V}_{ij} = \mathbb{I}[\Psi_i(\boldsymbol{\xi})\Psi_j(\boldsymbol{\xi})]$  being a numerical evaluation of  $\mathbb{E}[\Psi_i(\boldsymbol{\xi})\Psi_j(\boldsymbol{\xi})]$  using the quadrature points and weights from solving (11). We have

$$\|\mathbf{V} - I_{N_p}\|_F \le N_p T \epsilon. \tag{24}$$

*Proof:* See Appendix E. 
$$\Box$$

#### VI. NUMERICAL RESULTS

In order to show the efficiency of our proposed method, we conduct numerical experiments on a synthetic example, a three-stage CMOS electronic ring oscillator, and an optical filter. The stopping criterion in (11) is set as  $\epsilon=10^{-8}$  unless stated otherwise. In all examples, we use some Gaussian mixture models to describe the joint density functions of correlated non-Gaussian random parameters. The MATLAB codes and a demo example are provided online at https://web.ece.ucsb.edu/~zhengzhang/codes\_dataFiles/uq\_ng.

#### A. Synthetic Example

First, we consider a synthetic example and use it to show the accuracy and convergence rate of our proposed stochastic collocation algorithm. Specifically, we consider the following smooth function of two correlated parameters:

$$y(\xi) = \exp(\xi_1) + 0.1\cos(\xi_1)\sin(\xi_2).$$
 (25)

We assume that the random parameters follow a Gaussian mixture distribution

$$\boldsymbol{\xi} = \boldsymbol{\xi}_0 + \frac{1}{10}\Delta\boldsymbol{\xi}$$
, where  $\Delta\boldsymbol{\xi} \sim \frac{1}{2}\mathcal{N}(\boldsymbol{\mu}_1, \boldsymbol{\Sigma}_1) + \frac{1}{2}\mathcal{N}(\boldsymbol{\mu}_2, \boldsymbol{\Sigma}_2)$ .

Here, the mean values  $\mu_1 = 1$ ,  $\mu_2 = -1$ ; the positive-definite covariance matrices  $\Sigma_1$  and  $\Sigma_2$  are randomly generated. We use 1 to denote a vector of a compatible size with all elements being one. We will also use this notation in other examples.

We first illustrate how to generate the quadrature samples and weights by our optimization-based quadrature rule.

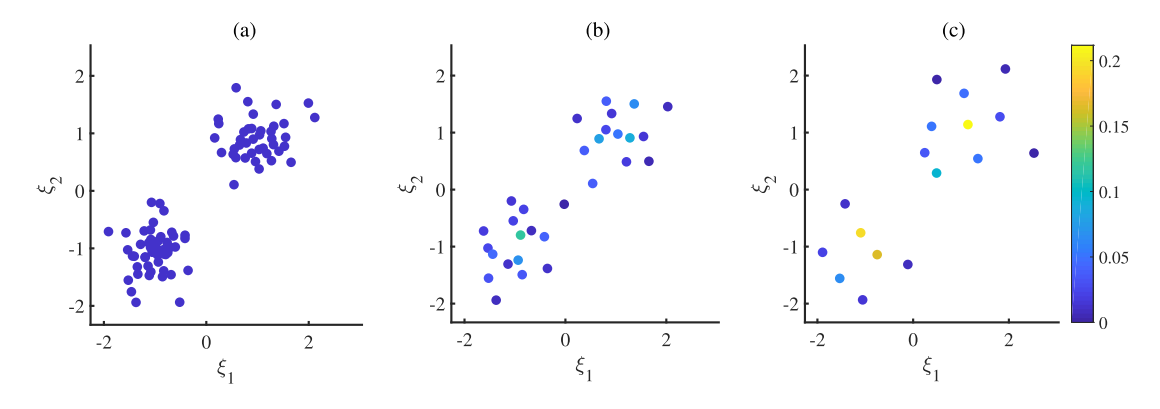


Fig. 2. Process of generating quadrature samples and weights for the synthetic example. The quadrature weights are shown by the color bar. (a) Initial candidate points generated via MC. (b) Clustered samples via the weighted complete-linkage method in Algorithm 3. (c) Optimized quadrature nodes by Algorithm 1. This process only depends on the probability density function and the basis functions and is independent of  $y(\xi)$ .

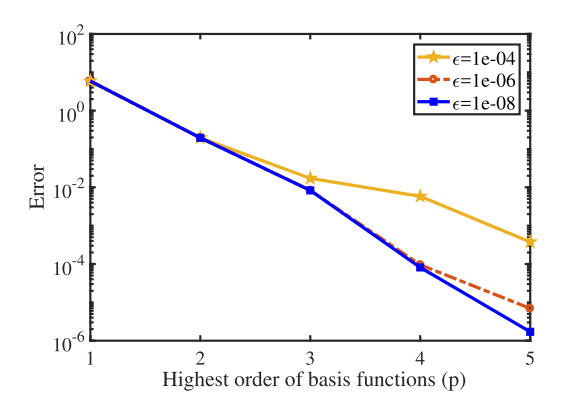


Fig. 3. Convergence rate for the synthetic example. Here,  $\epsilon$  is the numerical error of optimization defined in (21). This figure demonstrates the error estimated in (23): The stochastic collocation algorithm shows a nearly exponential convergence rate as p increases and before  $\epsilon$  dominates the error.

TABLE II

ACCURACY COMPARISON ON THE SYNTHETIC EXPERIMENTS.

THE UNDERSCORES INDICATE PRECISION

method	Proposed					
$\overline{}$	1	2	3	4	5	
# samples	3	6	10	17	66	
mean	2.7 <u>8</u> 35	2.782 <u>9</u>	2.782 <u>9</u>	2.782 <u>9</u>	2.782 <u>9</u>	
method	Monte Carlo			o		
# samples	10	$10^{2}$	$10^{3}$	$10^{4}$	$10^{5}$	
mean	2.6799	2.7625	2. <u>7</u> 911	2.7 <u>8</u> 11	2.782 <u>9</u>	

Assume that we want to approximate  $y(\xi)$  by a fourth-order expansion. First, 90 random samples are generated via MC. Second, these points are grouped into 30 clusters via our proposed weighted linkage clustering approach, and they are used as the initial samples and weights of Algorithm 1. Finally, the number of quadrature nodes is reduced to 17 automatically by Algorithm 1, whereas the lower bound for the number of quadrature nodes is 15. The process of generating quadrature samples and weights is shown in Fig. 2.

Theorem 4 shows that the error depends on two parts: the numerical error  $\epsilon$  of the optimization solver of our quadrature rule and the approximation error  $\delta$  by order-p basis functions. When p is small,  $||y(\xi) - y_p(\xi)||_2 \le \delta$  dominates the error.

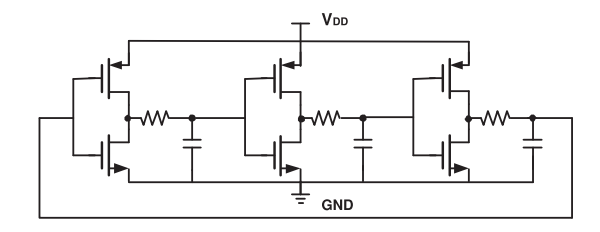


Fig. 4. Schematic of a three-stage CMOS ring oscillator.

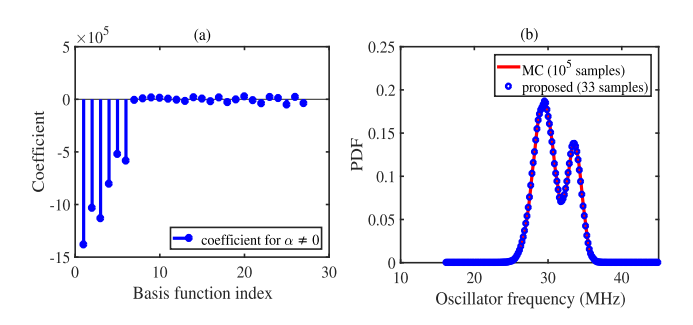


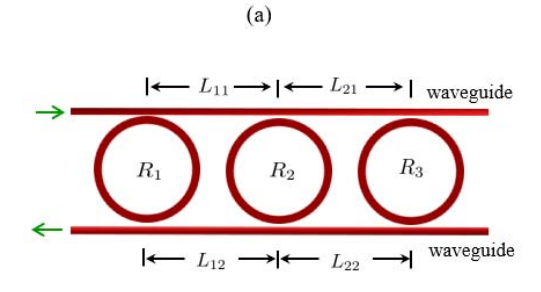
Fig. 5. Numerical results of the CMOS ring oscillator. (a) Obtained coefficients/weights of our basis functions. (b) Probability density functions of the oscillator frequency obtained by our proposed method and MC.

TABLE III
ACCURACY COMPARISON ON THE CMOS RING OSCILLATOR. THE
UNDERSCORES INDICATE PRECISION

method	Proposed	Monte Carlo			
# samples	33	$10^{2}$	$10^{3}$	$10^{4}$	$10^{5}$
mean (MHz)	30.83	30.93	30.88	30.80	30.83

When p is large,  $\delta$  becomes small and  $\epsilon$  dominates the error, and therefore, smaller  $\epsilon$  will produce more accurate results. In order to verify this theoretical result, we perform stochastic collocation by using different orders of basis functions (i.e., p=1-5) and by setting different error thresholds (i.e.,  $\epsilon=10^{-4}$ ,  $10^{-6}$ , and  $10^{-8}$ ) in the optimization-based quadrature rule. As shown in Fig. 3, our stochastic collocation has a nearly exponential convergence rate before  $\epsilon$  dominates the error.

We further compare our method with MC in Table II. Our method provides a closed-form expression for the mean value



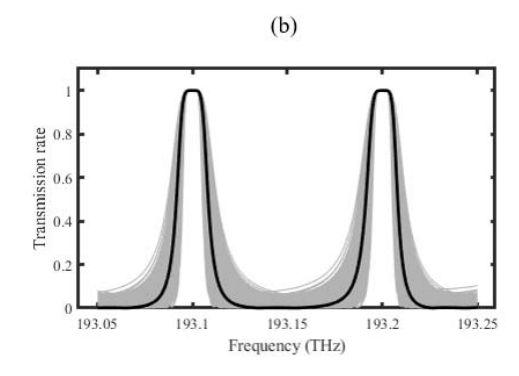


Fig. 6. (a) Schematic of a three-stage parallel-coupled ring resonator optical filter.  $L_{12}$ ,  $L_{21}$ ,  $L_{23}$ , and  $L_{32}$  are the connecting waveguides, and  $R_1$ ,  $R_2$ , and  $R_3$  denote the rings. (b) Black line shows the nominal transmission function, and the thin gray lines show the effect of fabrication uncertainties on the waveguide lengths of  $L_{12}$ ,  $L_{21}$ ,  $L_{23}$ , and  $L_{32}$ .

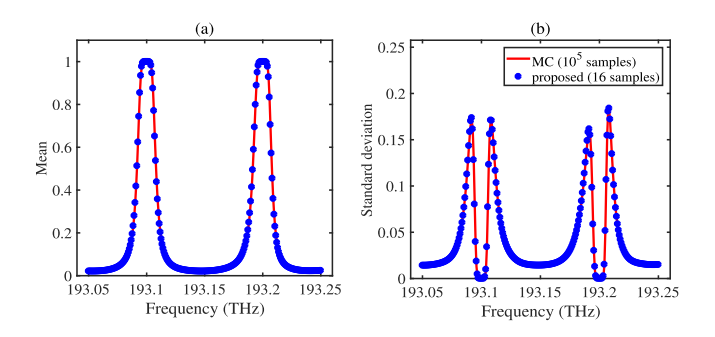


Fig. 7. Simulation results with respect to the geometric uncertainties in the waveguide length of  $L_{12}$ ,  $L_{21}$ ,  $L_{23}$ , and  $L_{32}$ . (a) Obtained mean value of the power transmission rate. (b) Standard deviation of the transmission rate.

of  $y(\xi)$ , and a second-order expansion using six quadrature points is sufficient to achieve a precision of four fractional digits. In contrast, MC requires  $10^5$  random samples to achieve a similar level of accuracy.

#### B. Three-Stage CMOS Electronic Ring Oscillator

We continue to verify our algorithm by the three-stage CMOS ring oscillator in Fig. 4. We model the relative threshold voltage variations of six transistors via

$$\boldsymbol{\xi} = \boldsymbol{\xi}_0 + \mathbf{D}\Delta\boldsymbol{\xi}, \text{ with } \Delta\boldsymbol{\xi} \sim \frac{2}{3}\mathcal{N}(\boldsymbol{\mu}_1, \boldsymbol{\Sigma}_1) + \frac{1}{3}\mathcal{N}(\boldsymbol{\mu}_2, \boldsymbol{\Sigma}_2)$$

where **D** is a diagonal scaling matrix,  $\mu_1 = 1$ ,  $\mu_2 = -1$ , and  $\Sigma_1$  and  $\Sigma_2$  are randomly generated positive-definite matrices.

We aim to approximate the frequency by a secondorder expansion of our multivariate basis functions. Our optimization-based quadrature rule generates 33 pairs of quadrature samples and weights, and then a deterministic periodic steady-state simulator is called repeatedly to simulate the oscillator at all parameter samples. Fig. 5 shows the obtained weights of all basis functions and the probability density function.

We compare the computed mean value from our methods with that from MC in Table III. The MC method converges very slowly and requires  $3030\times$  more simulation samples to achieve the similar level of accuracy (with two accurate fractional digits).

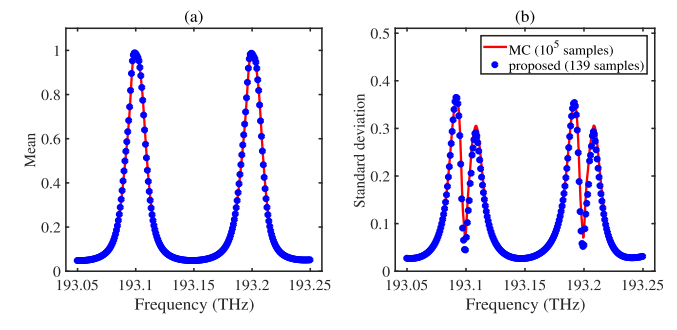


Fig. 8. Simulation results with respect to the geometric uncertainties in the waveguide length of  $L_{12}$ ,  $L_{21}$ ,  $L_{23}$ ,  $L_{32}$ ,  $R_{1}$ ,  $R_{2}$ , and  $R_{3}$ , and the uncertainties in effective index for  $L_{12}$ ,  $L_{21}$ ,  $L_{23}$ , and  $L_{32}$ . (a) Obtained mean value of the power transmission rate. (b) Standard deviation of the transmission rate.

#### C. Parallel-Coupled Ring Resonator Optical Filter

In this section, we consider the three-stage parallel-coupled ring resonator optical filter<sup>1</sup> in Fig. 6(a). This optical filter is a versatile component for wavelength filtering, multiplexing, switching, and modulation in photonic ICs. This circuit has a nominal 3-dB bandwidth of 12 GHz, and the coupling coefficients for the three rings are  $K_1 = K_3 = 0.198836$  and  $K_2 = 0.356423$ . In the nominal design, the waveguide lengths  $L_{12}$ ,  $L_{21}$ ,  $L_{23}$ , and  $L_{32}$  are all 30.6624  $\mu$ m, and the circumference of all rings is  $R_1 = R_2 = R_3 = 2997.92 \ \mu$ m. In practice, there exist non-Gaussian correlated uncertainties in the waveguide geometric parameters. The effect of fabrication uncertainties is shown in Fig. 6(b).

Our goal is to build a second-order stochastic model to approximate the power transmission curve at different frequency points  $y(f, \xi) = \sum_{|\alpha|=0}^{p} c_{\alpha}(f) \Psi_{\alpha}(\xi)$ . We use a Gaussian mixture model to describe the uncertainties

$$\boldsymbol{\xi} = \boldsymbol{\xi}_0 + \Delta \boldsymbol{\xi}$$
, where  $\Delta \boldsymbol{\xi} \sim \frac{1}{2} \mathcal{N}(\boldsymbol{\mu}_1, \boldsymbol{\Sigma}_1) + \frac{1}{2} \mathcal{N}(\boldsymbol{\mu}_2, \boldsymbol{\Sigma}_2)$ .

For the waveguide length parameters, we use

$$\mu_1 = -\mu_2 = 25 \times 1$$
nm,  $\Sigma_1 = \Sigma_2 = 6.25(I + 0.5E)$ .

<sup>1</sup>The details of this benchmark can be found at https://kb.lumerical.com/en/pic\_circuits\_coupled\_ring\_resonator\_filters.html.

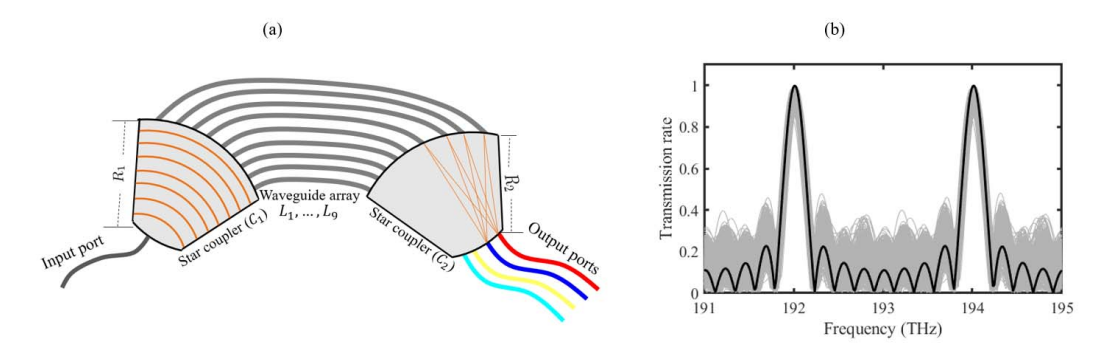


Fig. 9. (a) Schematic of an AWG with nine waveguide arrays. (b) Nominal transmission rate from the input to output Port 1. Black curve: result without any uncertainties. Gray lines: effects caused by the fabrication uncertainties of radius  $R_1$  and  $R_2$  and waveguide lengths  $L_1, \ldots, L_9$ .

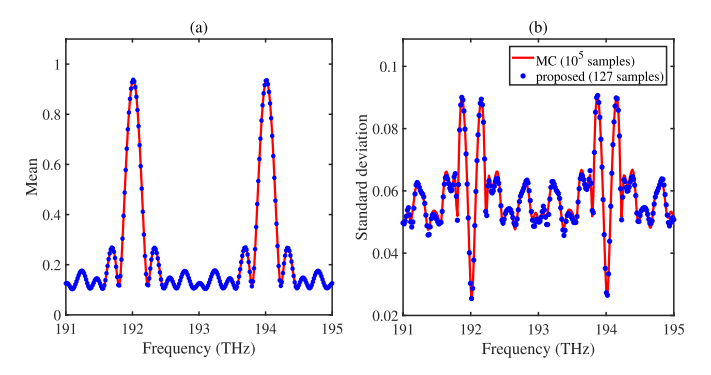


Fig. 10. Numerical results of the AWG with non-Gaussian correlated uncertainties in radius  $R_1$  and  $R_2$  and the waveguide array lengths of  $L_1, \ldots, L_9$ . (a) Mean value of the transmission rate. (b) Standard deviation of the transmission rate obtained by our proposed method and MC.

The uncertainties of the effective index follow a Gaussian mixture distribution with

$$\mu_1 = -\mu_2 = 10^{-3} \times 1$$
,  $\Sigma_1 = \Sigma_2 = 10^{-6} (I + 0.5E)$ .

We perform two experiments for the optical filter. The first experiment only considers the uncertainties of the waveguide lengths  $L_{12}$ ,  $L_{21}$ ,  $L_{23}$ , and  $L_{32}$ . The second experiments consider the uncertainties of the waveguide lengths  $L_{12}$ ,  $L_{21}$ , and  $L_{23}$ , ring geometry  $L_{32}$ ,  $R_1$ ,  $R_2$ , and  $R_3$ , as well as the effective index of  $L_{12}$ ,  $L_{21}$ ,  $L_{23}$ , and  $L_{32}$ . The mean value and the standard derivation of the output response are shown in Figs. 7 and 8, respectively. Although our method only uses 16 or 139 samples, it is able to achieve the similar accuracy with MC that consumes  $10^5$  simulation samples.

#### D. Arrayed Waveguide Grating

Finally, we consider an arrayed waveguide grating (AWG) [62]. The AWG is essential for wavelength division and multiplexing in photonic systems. In our experiment, we use an AWG with nine waveguide arrays and two star couplers, as shown in Fig. 9(a). In the nominal design, the radius of each star coupler is  $R_1 = R_2 = 2.985$  mm, and the waveguide lengths  $L_1, \ldots, L_9$  range from 46 to 420  $\mu$ m. In practice, there exist non-Gaussian correlated uncertainties in the device geometric parameters, and the resulting performance uncertainties are shown in Fig. 9(b).

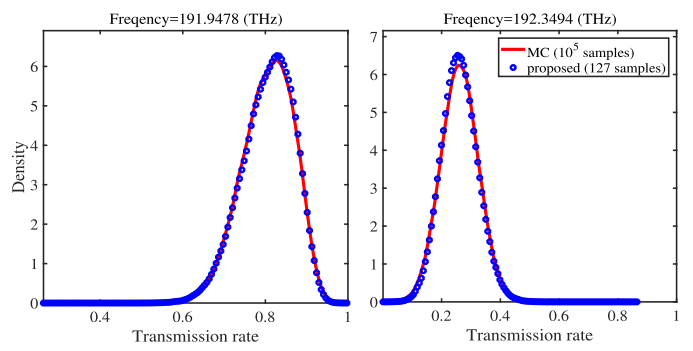


Fig. 11. Probability density functions of the transmission rates at two frequency points f=191.9478 THz and f=192.3494 THz obtained by our proposed method and MC.

We aim to build a second-order stochastic model to approximate the transmission rates. A Gaussian mixture model is used to describe the geometric uncertainties

$$\boldsymbol{\xi} = \boldsymbol{\xi}_0 + \Delta \boldsymbol{\xi}, \text{ where } \Delta \boldsymbol{\xi} \sim \frac{1}{2} \mathcal{N}(\boldsymbol{\mu}_1, \boldsymbol{\Sigma}_1) + \frac{1}{2} \mathcal{N}(\boldsymbol{\mu}_2, \boldsymbol{\Sigma}_2).$$

For the radius of the star couplers, we set the mean values as  $\mu_1 = -\mu_2 = 29.8 \times 1 \ \mu \text{m}$ . For the waveguide array lengths, we set  $\mu_1 = -\mu_2 = 0.05 \times 1 \ \mu \text{m}$ . The covariance matrices are block-diagonal positive definite.

We compare the computed mean value and standard deviation of our method with that from MC in Fig. 10. Using only 127 simulation samples, our method is able to achieve the similar accuracy with  $10^5$  MC samples. Fig. 11 further shows the probability density functions of the transmission rates at two frequency points f=191.9478 THz and f=192.3494 THz.

#### E. Practical Number of Quadrature Samples

Finally, Table IV shows the number of quadrature samples used by our approach in all numerical experiments. The lower and upper bounds of the number of samples from Theorem 1 are listed in the last two columns. Clearly, in most cases, the practical number of samples is very close to the lower bound. When the order of basis function is very high, the obtained number of quadrature samples may occasionally become close to the upper bound. This is because the following reason: When p is very large, the objective function in (11)

TABLE IV  $\begin{tabular}{ll} Number of Quadrature Samples Used in All Experiments. Here, \\ p Denotes the Maximal Order of Basis Functions and $d$ Is the \\ Number of Random Parameters \\ \end{tabular}$ 

			Proposed			
Benchmarks	p	d	# samples	lower bound	upper bound	
	1	2	3	3	6	
	2	2	6	6	15	
Synthetic	3	2	10	10	28	
	4	2	17	15	45	
	5	2	66	21	66	
CMOS ring	2	6	33	28	210	
Ontical filton	2	4	16	15	70	
Optical filter	2	11	139	78	1365	
AWG	2	11	127	78	1365	

is a polynomial function of extremely high order (i.e., 4p), and the coordinate descent solver becomes hard to converge. We expect that the number of quadrature samples will also be close to the theoretical lower bound even for very large p, if a better nonlinear optimization solver is developed in the future.

#### VII. CONCLUSION

This paper has investigated a long-standing research challenge: How can we handle non-Gaussian correlated uncertainties by stochastic spectral methods? We have proposed several theories and algorithms to overcome this challenge and have tested them by various benchmarks. Specifically, we have proposed a set of orthonormal basis functions that work extremely well for non-Gaussian correlated process variations, which are beyond the capability of the existing well-known generalized polynomial-chaos theory. We have presented an optimization approach to calculate the quadrature nodes and weights required in the projection step. We have also provided some rigorous theoretical results regarding the required number of quadrature samples and the error bound of our framework. Our method has demonstrated a nearly exponential convergence rate on a smooth synthetic example. It has also achieved  $700 \times -6000 \times$  speedup than MC on several practical design benchmarks, including a CMOS electronic ring oscillator, an optical filter built with three-stage photonic ring resonators, and an AWG.

We have two final remarks in the following.

- Based on our theoretical analysis, we conclude that as long as the stochastic unknown output is smooth enough, and if the optimization solver in our quadrature rule has a small error, both the numerical integration and the approximation error will be very small, leading to highly accurate results in our stochastic collocation framework.
- 2) It remains an open problem to determinate the required minimum number of quadrature nodes. Our numerical experiments show an excellent heuristic result: The practical number of quadrature nodes used in our framework is almost always close to the theoretical lower bound.

## APPENDIX A PROOF OF THEOREM 1

We show the lower bound and upper bounds of the number of quadrature points required to achieve 2pth-order accuracy are  $N_p$  and  $N_{2p}$ , respectively.

First, according to Appendix B, (29) holds if the quadrature points and weights satisfy (10). As a result, we have

$$\mathbf{Q}\mathrm{diag}(\mathbf{w})\mathbf{Q}^T = \mathbf{I}_{N_n} \tag{26}$$

where  $\mathbf{Q} \in \mathbb{R}^{N_p \times M}$  with each element  $\mathbf{Q}_{ij} = \Psi_i(\boldsymbol{\xi}_j)$  and  $\mathbf{I}_{N_p}$  is an  $N_p \times N_p$  identity matrix. Because the right-hand side is full rank,  $\mathbf{Q}$  has a full row rank and, thus,  $M \geq N_p$ .

We further notice that the first row of (10) is  $\sum_{k=1}^{M} w_k = 1$ , and therefore, (10) can be rewritten as

$$\mathbf{Q}_1 \mathbf{w} = \mathbf{0}_{N_{2p}-1}, \ \sum_{k=1}^{M} w_k = 1, \ \mathbf{w} \ge 0$$
 (27)

where  $\mathbf{Q}_1 \in \mathbb{R}^{(N_{2p}-1) \times M}$  consists of the last  $N_{2p}-1$  rows of  $\mathbf{Q}$  and  $\mathbf{0}_{N_{2p}-1} \in \mathbb{R}^{N_{2p}-1}$  is a zero vector. According to Carathéodory's theorem [63], because  $\mathbf{0}_{N_{2p}}$  lies in the convex hull formed by the column vectors of  $\mathbf{Q}_1$ , it can be written as the convex combination of not more than  $N_{2p}$  column vectors. In other words, there exists a matrix  $\hat{\mathbf{Q}}_1$  formed by only  $N_{2p}$  columns of  $\mathbf{Q}_1$ , such that (27) still holds if we replace  $\mathbf{Q}_1$  with  $\hat{\mathbf{Q}}_1$  and change the length of  $\mathbf{w}$  accordingly. Vector  $\mathbf{0}_{N_{2p}-1}$  being in the convex hull of  $\mathbf{Q}_1$  is a natural result of our numerical quadrature rule defined on the selected basis functions, and therefore, there exists  $M \leq N_{2p}$ .

Remark: In the above-mentioned proof, we show that by Carathéodory's theorem, there exist  $N_{2p}$  quadrature nodes and weights, such that (27) is true. In general, we do not know how to choose the  $N_{2p}$  sample nodes and weights a priori. However, our optimization solver can automatically calculate these quadrature nodes and weights. On the contrary, the linear programing approach in [56] needs to prescribe the sampling nodes and only calculate the weights, and it cannot guarantee the conditions in (27).

# APPENDIX B PROOF OF THEOREM 2

In order to show the exact recovery of  $y(\xi) \in \mathcal{S}_p$ , we need to prove that

$$c_{\alpha} = \tilde{c}_{\alpha} \quad \forall \ |\alpha| < p.$$
 (28)

Here,  $\tilde{c}_{\alpha}$  is obtained by the following numerical scheme:

$$\tilde{c}_{\alpha} = \sum_{k=1}^{M} y(\boldsymbol{\xi}_{k}) \Psi_{\alpha}(\boldsymbol{\xi}_{k}) w_{k} = \sum_{k=1}^{M} \sum_{|\boldsymbol{\beta}|=0}^{p} c_{\boldsymbol{\beta}} \Psi_{\boldsymbol{\beta}}(\boldsymbol{\xi}_{k}) \Psi_{\alpha}(\boldsymbol{\xi}_{k}) w_{k}$$
$$= \sum_{|\boldsymbol{\beta}|=0}^{p} c_{\boldsymbol{\beta}} \left( \sum_{k=1}^{M} \Psi_{\boldsymbol{\beta}}(\boldsymbol{\xi}_{k}) \Psi_{\alpha}(\boldsymbol{\xi}_{k}) w_{k} \right).$$

A sufficient condition of (28) is

$$\sum_{k=1}^{M} \Psi_{\beta}(\xi_k) \Psi_{\alpha}(\xi_k) w_k = \delta_{\alpha,\beta}. \tag{29}$$

In fact, the left-hand side of (29) is the numerical approximation for the integral  $\mathbb{E}[\Psi_{\beta}(\xi)\Psi_{\alpha}(\xi)]$ , which is guaranteed to be exact if we have a quadrature rule that can exactly evaluate the integration of every basis function bounded by order 2p. In other words, (10) is a sufficient condition for (29).

### APPENDIX C PROOF OF THEOREM 3

Before the detailed proof, we first introduce Hölder's inequality [64] that will be used in our theoretical analysis.

1) Hölder's Inequality for the Euclidean Vector Space: For all vectors  $\mathbf{x}, \mathbf{y} \in \mathbb{R}^n$  and  $q_1, q_2 \in [1, +\infty]$  with  $(1/q_1) + (1/q_2) = 1$ 

$$\left| \sum_{i=1}^{n} x_i y_i \right| \le \sum_{i=1}^{n} \left| x_i y_i \right| \le \|\mathbf{x}\|_{q_1} \|\mathbf{y}\|_{q_2}. \tag{30}$$

For the special case  $q_1 = 1$  and  $q_2 = +\infty$ , there is

$$\left| \sum_{i=1}^{n} x_i y_i \right| \le \sum_{i=1}^{n} |x_i y_i| \le \|\mathbf{x}\|_1 \|\mathbf{y}\|_{\infty}. \tag{31}$$

2) Hölder's Inequality in the Probability Space: For all measurable functions  $f(\xi)$  and  $g(\xi)$  and  $q_1, q_2 \in [1, +\infty]$  with  $(1/q_1) + (1/q_2) = 1$ 

$$\mathbb{E}[|f(\boldsymbol{\xi})g(\boldsymbol{\xi})|] \le ||f(\boldsymbol{\xi})||_{q_1} ||g(\boldsymbol{\xi})||_{q_2}. \tag{32}$$

For the special case  $g(\xi) \equiv 1$  and  $q_1 = q_2 = 2$ , there is

$$||f(\boldsymbol{\xi})||_1 = \mathbb{E}[|f(\boldsymbol{\xi})|] \le (\mathbb{E}[|f(\boldsymbol{\xi})|^2])^{\frac{1}{2}} = ||f(\boldsymbol{\xi})||_2.$$
 (33)

Now, we start to prove Theorem 3. According to the definition  $y_p(\xi) = \sum_{|\alpha|=0}^p c_\alpha \Psi_\alpha(\xi)$  and  $c_\alpha = \mathbb{E}[y(\xi)\Psi_\alpha(\xi)]$ , we have

$$\mathbb{E}[y(\boldsymbol{\xi})\Psi_j(\boldsymbol{\xi})] = \mathbb{E}[y_p(\boldsymbol{\xi})\Psi_j(\boldsymbol{\xi})] = c_j \quad \forall j = 1, \dots, N_p.$$
(34)

We consider j=1 and  $\Psi_1(\xi)=1$ , and then (34) indicates  $\mathbb{E}[y(\xi)]=\mathbb{E}[y_p(\xi)]=c_0$ . Based on this observation, we can estimate the difference between  $\mathbb{E}[y(\xi)]$  and  $\mathbb{I}[y(\xi)]$ 

$$|\mathbb{E}[y(\xi)] - \mathbb{I}[y(\xi)]|$$

$$= |\mathbb{E}[y_p(\xi)] - \mathbb{I}[y(\xi)]|$$

$$\leq |\mathbb{E}[y_p(\xi)] - \mathbb{I}[y_p(\xi)]| + |\mathbb{I}[y_p(\xi)] - \mathbb{I}[y(\xi)]|. \quad (35)$$

Item (a) arises from the error of our numerical quadrature

$$(a) = \left| \mathbb{E}[y_p(\boldsymbol{\xi})] - \mathbb{I}[y_p(\boldsymbol{\xi})] \right| = \left| \sum_{j=1}^{N_p} c_j \left( \mathbb{E}[\Psi_j(\boldsymbol{\xi})] - \mathbb{I}[\Psi_j(\boldsymbol{\xi})] \right) \right|$$

$$\leq \|\mathbf{c}\|_{\infty} \|\Phi(\bar{\boldsymbol{\xi}})\mathbf{w} - \mathbf{e}_1\|_1 \leq L\epsilon.$$
(36)

The first inequality results from Hölder's inequality (31). The second inequality follows from  $\|\Phi(\bar{\xi})\mathbf{w} - \mathbf{e}_1\|_1 \le \epsilon$  in (21), and we have  $\|\mathbf{c}\|_{\infty} \le L$  because

$$|c_i| = |\mathbb{E}[y(\xi)\Psi_i(\xi)]| \le ||y(\xi)||_2 ||\Psi_i(\xi)||_2 \le L ||\Psi_i(\xi)||_2 = L.$$

Item (b) is due to the projection error

$$(b) = |\mathbb{I}[y_p(\xi)] - \mathbb{I}[y(\xi)]| \leq W ||y(\xi) - y_p(\xi)||_1 \leq W ||y(\xi) - y_p(\xi)||_2 \leq W\delta.$$
 (37)

The first inequality follows from that the operator  $\mathbb{I}$  is bounded by W in (20). The second inequality results from Hölder's

inequality (33). The last inequality follows from our assumption  $||y(\xi) - y_p(\xi)||_2 \le \delta$  in (18).

Combining (35)–(37), we have

$$|\mathbb{E}[y(\xi)] - \mathbb{I}[y(\xi)]| \le L\epsilon + W\delta. \tag{38}$$

The proof of Theorem 3 is complete.

## APPENDIX D PROOF OF THEOREM 4

The total error of our stochastic collocation algorithm can be bounded by two terms

$$\|y(\xi) - \tilde{y}(\xi)\|_2 \le \|y(\xi) - y_p(\xi)\|_2 + \|y_p(\xi) - \tilde{y}(\xi)\|_2.$$

Based on Assumption 2, the first item is upper bounded by  $\delta$ . We only need to estimate the second term. In fact

$$\|y_p(\xi) - \tilde{y}(\xi)\|_2 = \|\sum_{j=1}^{N_p} (c_j - \tilde{c}_j) \Psi_j(\xi)\|_2 = \sqrt{\sum_{j=1}^{N_p} (c_j - \tilde{c}_j)^2}$$

where the last equality follows the fact that the chosen basis functions are orthogonal and normalized. Furthermore

$$|c_{j} - \tilde{c}_{j}| = |\mathbb{E}[y_{p}(\xi)\Psi_{j}(\xi)] - \mathbb{I}[y(\xi)\Psi_{j}(\xi)]|$$

$$\leq |\mathbb{E}[y_{p}(\xi)\Psi_{j}(\xi)] - \mathbb{I}[y_{p}(\xi)\Psi_{j}(\xi)]|$$

$$+ |\mathbb{I}[(y_{p}(\xi) - y(\xi))\Psi_{j}(\xi)]|.$$

$$(40)$$

Both  $y_p(\xi)$  and  $\Psi_j(\xi)$  are polynomials bounded by order p, so their product is a polynomial bounded by order 2p, i.e.,  $y_p(\xi)\Psi_j(\xi) \in \mathcal{S}_{2p}$ . There exists an expansion  $y_p(\xi)\Psi_j(\xi) = \sum_{l=1}^{N_{2p}} a_l \Psi_l(\xi)$  and an upper bound for term (a)

$$(a) = |\mathbb{E}[y_p(\boldsymbol{\xi})\Psi_j(\boldsymbol{\xi})] - \mathbb{I}[y_p(\boldsymbol{\xi})\Psi_j(\boldsymbol{\xi})]|$$

$$= \left|\sum_{l=1}^{N_{2p}} a_l \left(\mathbb{E}[\Psi_l(\boldsymbol{\xi})] - \mathbb{I}[\Psi_l(\boldsymbol{\xi})]\right)\right|$$

$$\leq \|\mathbf{a}\|_{\infty} \|\Phi(\bar{\boldsymbol{\xi}})\mathbf{w} - \mathbf{e}_1\|_1 \leq LT\epsilon. \tag{41}$$

The first inequality is due to (31), and the last inequality follows from

$$a_{l} = \mathbb{E}[y_{p}(\xi)\Psi_{j}(\xi)\Psi_{l}(\xi)] \le \|y_{p}(\xi)\|_{2} \|\Psi_{j}(\xi)\Psi_{l}(\xi)\|_{2} \le LT$$
(42)

where  $T = \max_{j,l=1,...,N_{2p}} \|\Psi_j(\xi)\Psi_l(\xi)\|_2$ .

We can also find an upper bound for term (b) in (40)

$$(b) = |\mathbb{I}[(y_{p}(\xi) - y(\xi))\Psi_{j}(\xi)]|$$

$$\leq W \|(y_{p}(\xi) - y(\xi))\Psi_{j}(\xi)\|_{1}$$

$$\leq W \|y_{p}(\xi) - y(\xi)\|_{2} \|\Psi_{j}(\xi)\|_{2}$$

$$= W \|y_{p}(\xi) - y(\xi)\|_{2} \leq W\delta. \tag{43}$$

Combining (39)–(41) and (43), we have  $|c_j - \tilde{c}_j| \le LT\epsilon + W\delta$ , and thus,  $\|y_p(\xi) - \tilde{y}(\xi)\|_2 \le N_p(LT\epsilon + W\delta)$ . Noting that  $\|y(\xi) - y_p(\xi)\|_2 \le \delta$ , we finally have

$$\|y(\xi) - \tilde{y}(\xi)\|_2 \le \delta + N_p(LT\epsilon + W\delta). \tag{44}$$

This completes the proof of Theorem 4.

*Remark:* The boundness of  $a_l$  in (42) is equivalent to the completeness of  $S_{2p}$  under the Minkowski sum, i.e.,

$$S_p \oplus S_p \subset S_{2p}.$$
 (45)

In other words, if  $p_1(\xi)$ ,  $p_2(\xi) \in \mathcal{S}_p$ , then  $p_1(\xi)p_2(\xi) \in \mathcal{S}_{2p}$ . Intuitively, this is true because the product of two pth-order polynomials is a polynomial bounded by order 2p. A sufficient condition for (45) is that  $\|\Psi_j(\xi)\Psi_l(\xi)\|_2$  is bounded. In real applications, most widely used distributions, including Gaussian, Gaussian mixture distribution, or a distribution on a bounded domain, can guarantee that the high-order moments are bounded. As a result, (45) holds in most cases. However, there exists some rare density functions whose high-order moments are not necessarily bounded, such as the lognormal distribution. In this rare case, the error analysis in Theorem 4 may not hold.

#### APPENDIX E PROOF FOR LEMMA 1

In order to upper-bound  $\|\mathbf{V} - \mathbf{I}_{N_p}\|_F$ , we consider the error for each element  $\mathbb{E}[\Psi_i(\boldsymbol{\xi})\Psi_j(\boldsymbol{\xi})] - \mathbb{I}[\Psi_i(\boldsymbol{\xi})\Psi_j(\boldsymbol{\xi})]$ . We can have an expansion  $\Psi_i(\boldsymbol{\xi})\Psi_j(\boldsymbol{\xi}) = \sum_{l=1}^{N_{2p}} a_l \Psi_l(\boldsymbol{\xi})$ , and then

$$\begin{split} &|\mathbb{E}[\Psi_{i}(\boldsymbol{\xi})\Psi_{j}(\boldsymbol{\xi})] - \mathbb{I}[\Psi_{i}(\boldsymbol{\xi})\Psi_{j}(\boldsymbol{\xi})]| \\ &= \left| \sum_{l=1}^{N_{2p}} a_{l} \left( \mathbb{E}[\Psi_{l}(\boldsymbol{\xi})] - \mathbb{I}[\Psi_{l}(\boldsymbol{\xi})] \right) \right| \\ &\leq \|\mathbf{a}\|_{2} \|\Phi(\bar{\boldsymbol{\xi}})\mathbf{w} - \mathbf{e}_{1}\|_{2}. \end{split}$$

Because 
$$\|\mathbf{a}\|_2^2 = \|\Psi_i(\boldsymbol{\xi})\Psi_j(\boldsymbol{\xi})\|_2^2 \le T^2$$
 and  $\|\Phi(\bar{\boldsymbol{\xi}})\mathbf{w} - \mathbf{e}_1\|_2 \le \|\Phi(\bar{\boldsymbol{\xi}})\mathbf{w} - \mathbf{e}_1\|_1 \le \epsilon$ 

we have

$$\left| \mathbb{E}[\Psi_i(\boldsymbol{\xi})\Psi_j(\boldsymbol{\xi})] - \mathbb{I}[\Psi_i(\boldsymbol{\xi})\Psi_j(\boldsymbol{\xi})] \right| \leq T\epsilon$$

and further obtain  $\|\mathbf{V} - \mathbf{I}_{N_p}\|_F \leq N_p T \epsilon$ .

#### ACKNOWLEDGMENT

The authors would like to thank the anonymous reviewers for their detailed comments. They would also like to thank A. Sadun, K. Zhang, and K. Liu for their helpful discussions on the benchmarks and on Lumerical interconnect and M. Gershman for his help on some of the code implementation. This paper was presented in [1] at the IEEE Conference on Electrical Performance of Electronic Packaging and Systems, San Jose, CA, USA, October 2018, and received the Best Conference Paper Award.

#### REFERENCES

- [1] C. Cui, M. Gershman, and Z. Zhang, "Stochastic collocation with non-Gaussian correlated parameters via a new quadrature rule," in *Proc. IEEE Conf. EPEPS*, San Jose, CA, USA, Oct. 2018, pp. 57–59.
- [2] D. S. Boning *et al.*, "Variation," *IEEE Trans. Semicond. Manuf.*, vol. 21, no. 1, pp. 63–71, Feb. 2008.
- [3] M. Miranda, "The threat of semiconductor variability," *IEEE Spectr.*, Jun. 2012.
- [4] S. K. Selvaraja, W. Bogaerts, P. Dumon, D. V. Thourhout, and R. Baets, "Subnanometer linewidth uniformity in silicon nanophotonic waveguide devices using CMOS fabrication technology," *IEEE J. Sel. Topics Quantum Electron.*, vol. 16, no. 1, pp. 316–324, Jan. 2010.

- [5] W. A. Zortman, D. C. Trotter, and M. R. Watts, "Silicon photonics manufacturing," Opt. Express, vol. 18, no. 23, pp. 23598–23607, Nov. 2010.
- [6] L. Chrostowski, X. Wang, J. Flueckiger, Y. Wu, Y. Wang, and S. T. Fard, "Impact of fabrication non-uniformity on chip-scale silicon photonic integrated circuits," in *Proc. Opt. Fiber Commun. Conf.*, 2014, pp. 1–3.
- [7] Z. Lu et al., "Performance prediction for silicon photonics integrated circuits with layout-dependent correlated manufacturing variability," Opt. Express, vol. 25, no. 9, pp. 9712–9733, 2017.
- [8] S. Weinzierl, "Introduction to Monte Carlo methods," NIKHEF, Theory Group, Amsterdam, The Netherlands, Tech. Rep. NIKHEF-00-012, 2000
- [9] D. Xiu, Numerical Methods for Stochastic Computations: A Spectral Method Approach. Princeton, NJ, USA: Princeton Univ. Press, 2010.
- [10] D. Xiu and G. E. Karniadakis, "The Wiener-Askey polynomial chaos for stochastic differential equations," SIAM J. Sci. Comput., vol. 24, no. 2, pp. 619–644, Feb. 2002.
- [11] R. G. Ghanem and P. Spanos, Stochastic Finite Elements: A Spectral Approach. New York, NY, USA: Springer-Verlag, 1991.
- [12] Z. Zhang, T. A. El-Moselhy, I. M. Elfadel, and L. Daniel, "Stochastic testing method for transistor-level uncertainty quantification based on generalized polynomial chaos," *IEEE Trans. Comput.-Aided Design Integr. Circuits Syst.*, vol. 32, no. 10, pp. 1533–1545, Oct. 2013.
- [13] D. Xiu and J. S. Hesthaven, "High-order collocation methods for differential equations with random inputs," SIAM J. Sci. Comput., vol. 27, no. 3, pp. 1118–1139, Mar. 2005.
- [14] S. Vrudhula, J. M. Wang, and P. Ghanta, "Hermite polynomial based interconnect analysis in the presence of process variations," *IEEE Trans. Comput.-Aided Design Integr. Circuits Syst.*, vol. 25, no. 10, pp. 2001–2011, Oct. 2006.
- [15] T.-A. Pham, E. Gad, M. S. Nakhla, and R. Achar, "Decoupled polynomial chaos and its applications to statistical analysis of high-speed interconnects," *IEEE Trans. Compon., Packag., Manuf. Technol.*, vol. 4, no. 10, pp. 1634–1647, Oct. 2014.
- [16] I. S. Stievano, P. Manfredi, and F. G. Canavero, "Parameters variability effects on multiconductor interconnects via Hermite polynomial chaos," *IEEE Trans. Compon., Packag., Manuf. Technol.*, vol. 1, no. 8, pp. 1234–1239, Aug. 2011.
- [17] K. Strunz and Q. Su, "Stochastic formulation of SPICE-type electronic circuit simulation with polynomial chaos," ACM Trans. Model. Comput. Simul., vol. 18, no. 4, pp. 15:1–15:23, Sep. 2008.
- [18] R. Pulch, "Modelling and simulation of autonomous oscillators with random parameters," *Math. Comput. Simul.*, vol. 81, no. 6, pp. 1128–1143, Feb. 2011.
- [19] M. R. Rufuie, E. Gad, M. Nakhla, R. Achar, and M. Farhan, "Fast variability analysis of general nonlinear circuits using decoupled polynomial chaos," in *Proc. Workshop Signal Power Integr.*, May 2014, pp. 1–4.
- [20] P. Manfredi, D. Vande Ginste, D. De Zutter, and F. G. Canavero, "Sto-chastic modeling of nonlinear circuits via SPICE-compatible spectral equivalents," *IEEE Trans. Circuits Syst. I, Reg. Papers*, vol. 61, no. 7, pp. 2057–2065, Jul. 2014.
- [21] Z. Zhang, T. A. El-Moselhy, P. Maffezzoni, I. M. Elfadel, and L. Daniel, "Efficient uncertainty quantification for the periodic steady state of forced and autonomous circuits," *IEEE Trans. Circuits Syst. II, Exp. Briefs*, vol. 60, no. 10, pp. 687–691, Oct. 2013.
- [22] M. Ahadi and S. Roy, "Sparse linear regression (SPLINER) approach for efficient multidimensional uncertainty quantification of high-speed circuits," *IEEE Trans. Comput.-Aided Design Integr. Circuits Syst.*, vol. 35, no. 10, pp. 1640–1652, Oct. 2016.
- [23] A. C. Yücel, H. Bagci, and E. Michielssen, "An ME-PC enhanced HDMR method for efficient statistical analysis of multiconductor transmission line networks," *IEEE Trans. Compon., Packag., Manuf. Technol.*, vol. 5, no. 5, pp. 685–696, May 2015.
- [24] Z. Zhang et al., "Stochastic testing simulator for integrated circuits and MEMS: Hierarchical and sparse techniques," in Proc. IEEE Custom Integr. Circuits Conf., Sep. 2014, pp. 1–8.
- [25] Z. Zhang, X. Yang, I. V. Oseledets, G. E. Karniadakis, and L. Daniel, "Enabling high-dimensional hierarchical uncertainty quantification by ANOVA and tensor-train decomposition," *IEEE Trans. Comput.-Aided Design Integr. Circuits Syst.*, vol. 34, no. 1, pp. 63–76, Jan. 2015.
- [26] T.-W. Weng, Z. Zhang, Z. Su, Y. Marzouk, A. Melloni, and L. Daniel, "Uncertainty quantification of silicon photonic devices with correlated and non-Gaussian random parameters," *Opt. Express*, vol. 23, no. 4, pp. 4242–4254, Feb. 2015.
- [27] A. Waqas, D. Melati, P. Manfredi, and A. Melloni, "Stochastic process design kits for photonic circuits based on polynomial chaos augmented macro-modelling," *Opt. Express*, vol. 26, no. 5, pp. 5894–5907, 2018.

- [28] Z. Zhang, T.-W. Weng, and L. Daniel, "Big-data tensor recovery for high-dimensional uncertainty quantification of process variations," *IEEE Trans. Compon.*, *Packag., Manuf. Technol.*, vol. 7, no. 5, pp. 687–697, May 2017.
- [29] X. Li, "Finding deterministic solution from underdetermined equation: Large-scale performance variability modeling of analog/RF circuits," *IEEE Trans. Comput.-Aided Design Integr. Circuits Syst.*, vol. 29, no. 11, pp. 1661–1668, Nov. 2010.
- [30] X. Yang, M. Choi, G. Lin, and G. E. Karniadakis, "Adaptive ANOVA decomposition of stochastic incompressible and compressible flows," *J. Comput. Phys.*, vol. 231, no. 4, pp. 1587–1614, 2012.
- [31] X. Ma and N. Zabaras, "An adaptive high-dimensional stochastic model representation technique for the solution of stochastic partial differential equations," J. Comput. Phys., vol. 229, no. 10, pp. 3884–3915, 2010.
- [32] T. El-Moselhy and L. Daniel, "Stochastic dominant singular vectors method for variation-aware extraction," in *Proc. Design Automat. Conf.*, 2010, pp. 667–672.
- [33] T. El-Moselhy and Luca Daniel, "Variation-aware interconnect extraction using statistical moment preserving model order reduction," in *Proc. Design, Automat. Test Eur. Conf. Exhib.*, 2010, pp. 453–458.
- [34] J. Pond et al., "Predicting the yield of photonic integrated circuits using statistical compact modeling," Proc. SPIE, vol. 10242, p. 102420S, May 2017.
- [35] H. Chang and S. S. Sapatnekar, "Statistical timing analysis considering spatial correlations using a single PERT-like traversal," in *Proc. Int.* Conf. Comput.-Aided Design, 2003, pp. 621–625.
- [36] S. Bhardwaj, S. Vrudhula, P. Ghanta, and Y. Cao, "Modeling of intra-die process variations for accurate analysis and optimization of nano-scale circuits," in *Proc. 43rd ACM/IEEE Design Automat. Conf.*, Jul. 2006, pp. 791–796.
- [37] S. S. Sapatnekar, "Overcoming variations in nanometer-scale technologies," *IEEE J. Emerg. Sel. Topics Circuits Syst.*, vol. 1, no. 1, pp. 5–18, Mar. 2011.
- [38] M. Rosenblatt, "Remarks on a multivariate transformation," Ann. Math. Statist., vol. 23, no. 3, pp. 470–472, 1952.
- [39] C. Soize and R. Ghanem, "Physical systems with random uncertainties: Chaos representations with arbitrary probability measure," SIAM J. Sci. Comput., vol. 26, no. 2, pp. 395–410, 2004.
- [40] G. H. Golub and J. H. Welsch, "Calculation of Gauss quadrature rules," Math. Comput., vol. 23, no. 106, pp. 221–230, 1969.
- [41] Y. Xu, "Optimal points for cubature rules and polynomial interpolation on a square," in Contemporary Computational Mathematics—A Celebration of the 80th Birthday of Ian Sloan. Springer, 2018, pp. 1287–1305.
- [42] J. A. Paulson, E. A. Buehler, and A. Mesbah, "Arbitrary polynomial chaos for uncertainty propagation of correlated random variables in dynamic systems," *IFAC-PapersOnLine*, vol. 50, no. 1, pp. 3548–3553, 2017.
- [43] M. Navarro, J. Witteveen, and J. Blom. (2014). "Polynomial chaos expansion for general multivariate distributions with correlated variables." [Online]. Available: https://arxiv.org/abs/1406.5483
- [44] Z. Liu and Y. Choe. (2018). "Data-driven sensitivity indices for models with dependent inputs using the polynomial chaos expansion." [Online]. Available: https://arxiv.org/abs/1803.10978
- [45] F. Nobile, R. Tempone, and C. G. Webster, "A sparse grid stochastic collocation method for partial differential equations with random input data," SIAM J. Numer. Anal., vol. 46, no. 5, pp. 2309–2345, 2008.
- [46] I. Babuška, F. Nobile, and R. Tempone, "A stochastic collocation method for elliptic partial differential equations with random input data," SIAM J. Numer. Anal., vol. 45, no. 3, pp. 1005–1034, 2007.
- [47] F. Nobile, R. Tempone, and C. G. Webster, "An anisotropic sparse grid stochastic collocation method for partial differential equations with random input data," SIAM J. Numer. Anal., vol. 46, no. 5, pp. 2411–2442, 2008.
- [48] W. Gautschi, "On generating orthogonal polynomials," SIAM J. Sci. Stat. Comput., vol. 3, no. 3, pp. 289–317, 1982.
- [49] T. Gerstner and M. Griebel, "Numerical integration using sparse grids," Numer. Algorithms, vol. 18, pp. 209–232, Mar. 1998.
- [50] H. Zhu, X. Zeng, W. Cai, J. Xue, and D. Zhou, "A sparse grid based spectral stochastic collocation method for variations-aware capacitance extraction of interconnects under nanometer process technology," in *Proc. Design, Automat. Test Eur. Conf. Exhib.*, Apr. 2007, pp. 1–6.
- [51] V. Barthelmann, E. Novak, and K. Ritter, "High dimensional polynomial interpolation on sparse grids," Adv. Comput. Math., vol. 12, no. 4, pp. 273–288, Mar. 2000.
- [52] Y. Xu, "On multivariate orthogonal polynomials," SIAM J. Math. Anal., vol. 24, no. 3, pp. 783–794, 1993.

- [53] R. Barrio, J. M. Peña, and T. Sauer, "Three term recurrence for the evaluation of multivariate orthogonal polynomials," *J. Approx. Theory*, vol. 162, no. 2, pp. 407–420, 2010.
- [54] G. H. Golub and C. F. van Loan, *Matrix Computations*, vol. 3. Baltimore, MD, USA: JHU Press, 2012.
- [55] C. Cui and Z. Zhang, "Uncertainty quantification of electronic and photonic ICs with non-Gaussian correlated process variations," in *Proc. Int. Conf. Comput.-Aided Design*, San Diego, CA, USA, Nov. 2018, p. 97.
- [56] E. K. Ryu and S. P. Boyd, "Extensions of Gauss quadrature via linear programming," Found. Comput. Math., vol. 15, no. 4, pp. 953–971, 2015.
- [57] V. Keshavarzzadeh, R. M. Kirby, and A. Narayan, "Numerical integration in multiple dimensions with designed quadrature," SIAM J. Sci. Comput., vol. 40, no. 4, pp. A2033–A2061, 2018.
- [58] R. Tappenden, P. Richtárik, and J. Gondzio, "Inexact coordinate descent: Complexity and preconditioning," *J. Optim. Theory Appl.*, vol. 170, no. 1, pp. 144–176, 2016.
- [59] J. B. Lasserre, "Global optimization with polynomials and the problem of moments," SIAM J. Optim., vol. 11, no. 3, pp. 796–817, 2001.
- [60] J. Nocedal and S. J. Wright, "Numerical optimization," in Springer Series in Operations Research and Financial Engineering. New York, NY, USA: Springer, 2006.
- [61] A. K. Jain, M. N. Murty, and P. J. Flynn, "Data clustering: A review," ACM Comput. Surv., vol. 31, no. 3, pp. 264–323, Sep. 1999.
- [62] K. Zhang, X. Xiao, Y. Zhang, and S. J. B. Yoo, "Verilog—A compact modeling and simulation of AWGR based all-to-all optical interconnects," in *Proc. CLEO*, Appl. Technol., 2018, Paper JW2A-49.
- [63] I. Bárány and R. Karasev, "Notes about the carathéodory number," Discrete Comput. Geometry, vol. 48, no. 3, pp. 783–792, 2012.
- [64] K. Kuttler, An Introduction to Linear Algebra. Provo, UT, USA: Brigham Young Univ., 2007.



Chunfeng Cui received the Ph.D. degree in computational mathematics from the Chinese Academy of Sciences, Beijing, China, in 2016, with a specialization in numerical optimization.

From 2016 to 2017, she was a Post-Doctoral Fellow with the City University of Hong Kong, Hong Kong. In 2017, she joined the Department of Electrical and Computer Engineering, University of California at Santa Barbara, Santa Barbara, CA, USA, as a Post-Doctoral Scholar. Since 2011, her research activity has been mainly focused in the

areas of tensor analysis and its applications. She has been working on numerical optimization algorithms for tensor problems, and its applications for machine learning and for uncertainty quantification of nanoscale chip design.

Dr. Cui received the Best Paper Award of the IEEE EPEPS 2018.



**Zheng Zhang** (M'15) received the Ph.D. degree in electrical engineering and computer science from the Massachusetts Institute of Technology (MIT), Cambridge, MA, USA, in 2015.

He is currently an Assistant Professor of electrical and computer engineering with the University of California at Santa Barbara (UCSB), Santa Barbara, CA, USA. His current research interests include uncertainty quantification with applications to the design automation of multidomain systems, such as nanoscale electronics, integrated

photonics, and autonomous systems, and tensor computational methods for high-dimensional data analytics. His industrial experiences include Coventor Inc. and Maxim-IC; academic visiting experiences include UCSB; Brown University, Providence, Rhode Island; and the Politechnico di Milano, Milan, Italy; and government lab experiences include Argonne National Labs.

Dr. Zhang received the Best Paper Award of the IEEE TRANSACTIONS ON COMPUTER-AIDED DESIGN OF INTEGRATED CIRCUITS AND SYSTEMS in 2014, the Best Paper Award of the IEEE TRANSACTIONS ON COMPONENTS, PACKAGING, AND MANUFACTURING TECHNOLOGY in 2018, two best paper awards, the IEEE EPEPS 2018 and the IEEE SPI 2016, and three additional best paper nominations, CICC 2014, ICCAD 2011, and ASP-DAC 2011, at international conferences. He was a recipient of the Li Ka-Shing Prize from The University of Hong Kong in 2011. His Ph.D. dissertation was recognized by the ACM SIGDA Outstanding Ph.D. Dissertation Award in Electronic Design Automation in 2016 and the Doctoral Dissertation Seminar Award (i.e., Best Thesis Award) from the Microsystems Technology Laboratory, MIT, in 2015.